# Particle sedimentation in a fluid at low Reynolds number: a generalization of hindered settling described by a two-phase continuum model.

C. Huber, E.M. Parmentier, and D. Florez

Department of Earth, Environmental and Planetary Sciences, Brown University, RI, USA

**Abstract**

Particle-fluid separation by settling is an ubiquitous process in Earth and Planetary Sciences. The rate of growth and the initial structure of cumulate layers in magma oceans or, over smaller scales, crustal magmatic systems depend on the crystal settling dynamics in melt-rich environments. The settling velocity of particles is controlled by a balance between buoyancy (contrast in density between phases) and drag forces. Since the seminal work of G. Stokes more than a century ago, parameterizations for the reduction of particle velocities caused by viscous dissipation due to their mutual interaction (hindrance) have commonly been described by a non-linear mapping between particle volume fraction and average particle settling velocity. In the present study we argue that these parameterizations neglect important physical behavior at high particle volume fractions, and as such are appropriate only when considering suspensions in which the particle volume fraction does not evolve dynamically in space or time. We introduce a more general model that accounts for the energy dissipation caused by changes in local particle volume fraction. This correction to hindered settling introduces a new term in the force balance (momentum conservation) that takes a similar form to compaction terms in two phase models at higher particle volume fraction and introduces a new consolidation or compaction viscosity that measures the resistance of the suspension to changes in solid volume fraction. Using idealized geometric models based on first principles, we derive closure equations for this effective compaction viscosity under both dilute and concentrated particle volume fraction limits. Through a series of numerical simulations, we show that the extended hindered settling model predicts two significant differences compared to traditional hindered settling models. First, while the steepening of particle volume fraction fronts observed with uncorrected settling remains, a dynamic instability (waves) is also generated at the front and travels at a slower velocity than the predicted hindered settling. This resolves the nonphysical, discontinuous behavior reflected by such fronts. Second, the rate of growth and structure of a cumulate layer growing above a no-flux (solid) boundary is strongly affected by the new compaction-like term of the model. In particular, the corrected model predicts the trapping of a higher volume fraction of interstitial melt in a correspondingly thicker cumulate layer.

## Key points

1. A new model for particle settling proposed includes the effect of energy dissipation caused by solid volume fraction changes of the suspension in time and space that is not accounted for in traditional hindered settling.
2. The predicted settling velocities are significantly reduced compared to traditional models, especially when heterogeneous suspensions are considered.
3. The new model also introduces waves in particle volume fraction at oversteepening fronts that travel at a slower velocity than the discontinuous front predicted by hindered settling alone.

## 1. Introduction

The settling of particles in a fluid is a ubiquitous natural process. From sediments accumulating on a river or seabed (for low viscosity fluids) to the separation of crystals in melts in magma oceans or magma chambers, the processes governing the rate of fluid/solid separation by gravity have been studied for over 170 years.

The rate of particle settling and its dependence on the volume fraction of suspended particles exerts a fundamental control on the sedimentation rate and by extension on the porosity structure of the growing, sedimented layer. An analytical solution exists for the separation velocity of a single spherical particle in a boundless fluid otherwise at rest since the pioneering work of Gabriel Stokes in 1851 (section IV of “On the effect of internal friction of fluids on the motion of pendulums”). Particle settling, however, even at low particle volume fractions, is a difficult non-linear problem that does not admit analytical solutions. Therefore, most work focused on unraveling the rate of settling within a suspension (hindered settling) relies on empirical laws often inferred from experiments or tested experimentally under idealized conditions (e.g. Richardson and Zaki, 1954).

A common feature to all hindered settling models is the assumption of the existence of a unique mapping between the hindrance factor, which describes the reduction of the rate of settling for a given particle shape and size and for the volume fraction of suspended particles. The dependence of settling rate on particle volume fraction is generally cast in a power-law relationship. A variety of parameterizations have been provided from different studies (see review of Davis and Acrivos, 1985), some of these models include a critical volume fraction of particles beyond which settling is stopped (jamming conditions, e.g. Faroughi and Huber 2015) while others assume a finite separation velocity for any finite fluid fraction (e.g. Richardson and Zaki, 1954). These parameterizations have been used widely in many areas of the Earth and

planetary sciences for decades and therefore have had a large impact on our field as quickly summarized in the following paragraphs.

Particle settling plays a major role on sedimentation. Sedimentary deposits are commonly used as archives of past environmental conditions. Interrogating these archives through geochemical and textural analyses generally requires estimates of sedimentation rates as well as means to assess whether these archives are reliable and not overprinted by, for example, diagenetic processes. Sediments accumulated at the ocean bottom are often highly porous (small solid fraction) and it is not uncommon for the porosity to be significantly greater than 0.5 (Moore, 1989; Dasgupta and Mukherjee, 2020). Ultimately, the porosity profile of the shallow sediments is controlled by (1) the deposition environment (composition and types of sediments) and the particle settling rate and (2) the reorganization of the porosity by consolidation shortly after deposition, both of which will be impacted by the corrected hindered settling model presented here.

In magmatic environments, settling is important to both bubble and crystal separation in the host melt (Marsh and Maxey, 1985; Martin and Nokes, 1989; Bergantz and Ni, 1999; Culha et al., 2020). Bubble-rich layers in laFor example, it is now well-accepted that crystal-melt separation is required to generate differentiated magmas (Bachmann and Bergantz, 2004; Hildreth and Wilson, 2007; Bachmann and Huber, 2016). The recent study of Lee and Morton (2015) argued based on the thermal longevity of intrusions and geochemistry that the crystal-melt separation that formed the high-silica granites in the Peninsular Range Batholiths (California) was largely influenced by hindered settling.

As in igneous intrusions, crystal sedimentation has been thought to play a major role in the evolution of early global scale magma oceans expected to form as planets accrete (Solomatov 2000). This early evolution may have important consequences for long term planetary evolution. A progressively increasing Fe content, and thus increasing density of mafic mineral phases that crystallize from the residual liquid, would create unstable compositional stratification of mantle cumulates causing mantle overturn (Boukare et al. 2018; Elkins Tanton 2012; Hess and Parmentier, 1995) and redistribution of trapped melt in cumulates. Incompatible element concentrations due to melt that freezes into the cumulates control mantle trace element variability and radiogenic heat production which can influence planetary evolution on time scales much longer than that of magma ocean solidification. Moreover, settling and consolidation of liquid metal droplets in a magma ocean and possibly through partially molten silicate cumulates may form metallic cores (e.g. Rubie et al. 2003; Stevenson, 1990). Buoyancy resulting from the competition between settling and convective mixing can control convective motions in solidifying core. Iron snow in planetary cores has been proposed as a mechanism to drive core convection and generate planetary magnetic dynamos. Huguet, et al. (2023) provide a recent summary of work relating to this process.

In this study, we revisit a major assumption underlying past treatments of hindered settling, specifically the existence of a unique relationship between particle volume fraction and settling

velocity. We argue that this assumption is valid only for suspensions that remain homogeneous (in terms of volume fraction) at all times. This is a serious limitation as these conditions are not satisfied for many applications of interest.

We develop a continuum framework based on two-phase theory to generalize the analysis of hindered settling to heterogeneous suspensions and most importantly the dynamic behavior of suspensions that develop heterogeneities in particle volume fraction over time. We find that while the standard models of hindered settling account for energy dissipation through the average drag between settling particles and the ambient viscous fluid, they do not account for the contribution of fluid drainage or accumulation when the volume fraction changes dynamically. We develop a general two-phase model that corrects hindered settling to account for the momentum dissipated by changes in local volume fraction. This model introduces a compaction-like consolidation viscosity (hereafter referred to as compaction viscosity), which depends on the fluid's viscosity and the local particle volume fraction. We derive three constitutive models to provide closure for the compaction viscosity and use the models to study the effect of this new, compaction-like, term on the settling rate of particles and the porosity structure of the resulting growing sediment layer form by the accumulation of particles. We compare our new model to the published, uncorrected, versions of hindered settling.

## 2. Model Formulation

### 2.1. Governing equations

Hindered settling is generally approached assuming that the ambient fluid is at rest or experiences a uniform velocity field (Richardson and Zaki, 1941; Bachelor, 1970; Guazzelli and Morris, 2012; Faroughi and Huber, 2015). Through a careful choice in reference frame (e.g. selecting that of the ambient fluid for example) and assuming an empirical description of the particles hindered velocity that depends only on the solid fraction *X*

$$V_H(X) = V_{st}H(X) \tag{1}$$

where $V_H$ is the hindered velocity, $V_{st}$ represents the Stokes velocity for a single particle and $H(X)$ is the hindrance function ($0 \leq H(X) \leq 1$). Here, mass conservation is written as

$$\frac{\partial \mathrm{X}}{\partial t} + \frac{\partial [\mathrm{X}\, V_H]}{\partial z} = \Omega. \tag{2}$$

In this expression $\Omega$ is either null or includes effects such as subgrid scale dispersion of particles (below the scale of the representative elementary volume) or particle mass changes (growth, resorption).

We posit here that the modeling of hindered settling processes in a general way using equation (2) is flawed, built upon an assumption that does not fully account for the effects of heterogeneous particle distributions in space and time. This is because the empirical definition of $V_H$ relies on the assumption that the particle volume fraction field is homogeneous in space (fixed and homogeneous X). We show below that accounting for spatial and temporal

heterogeneities in particle volume fraction requires a two-phase approach and, specifically, should include a correction on the stress acting on the particle field.

Starting from the framework of two-phase theory (Drew, 1983; McKenzie 1984; Bercovici, et al. 2001; Guazzelli and Morris, 2012; Wallis, 2020) we introduce 1-D mass conservation statements (z along gravity) for the fluid

$$\frac{\partial(1-X)}{\partial t} = -\frac{\partial\left((1-X)\,V_f\right)}{\partial z} \tag{3}$$

and solid

$$\frac{\partial X}{\partial t} = -\frac{\partial[X\,V_s]}{\partial z} \tag{4}$$

assuming no mass exchange or source/sink in the system. $V_f$ and $V_s$ are the volume averaged vertical (z) velocity component of the fluid (index f) or solid (s) fraction, respectively.

Neglecting inertia, the momentum conservation equations acting on each phase reads

$$\frac{\partial\left((1-X)\sigma_{zz}^{f}\right)}{\partial z} + (1-X)\rho_f g - I = 0 \tag{5}$$

and

$$\frac{\partial[X\,\sigma_{zz}^{s}]}{\partial z} + \mathrm{X}\,\rho_s g + I = 0 \tag{6}$$

where $\sigma_{zz}$ is the vertical normal stress acting on the phase, $\rho_x$ is the density of a given phase and I is the interphase force (normal + tangential force acting at interfaces). Here, the interphase force is written as

$$I = c\left(V_f - V_s\right) - P_f\frac{\partial(1-X)}{\partial z} \tag{7}$$

where $c$ is a drag coefficient and $P_f$ is the average fluid pressure. The difference of velocity between the solid and fluid phase is generally considered as the hindered velocity

$$V_H = V_s - V_f. \tag{8}$$

We define the normal vertical stress acting on the particles to be a perturbation to the fluid's normal stress (where deviatoric stresses are neglected, i.e. $\sigma_{zz}^{f} = -P_f$)

$$\sigma_{zz}^{s} = \sigma_{zz}^{f} + \Delta\sigma = -P_f + \Delta\sigma. \tag{9}$$

The perturbation Δσ represents the additional stress acting on particles associated with the development of heterogeneities in the fluid/particle volume fractions. The development of such heterogeneities requires work to be performed to increase or decrease the particle volume fraction locally by draining interstitial fluid out of or into the control volume of interest. A generic parameterization for Δσ is

$$\Delta\sigma = \zeta \frac{\partial V_s}{\partial z}. \quad (10)$$

The scaling term in front of the divergence of the average particle velocity field has units of a viscosity and mirrors the definition of a compaction stress and viscosity. While this parameterization is similar to a compaction stress, it is easy to show that the material property ζ is a function of the local particle volume fraction, permeability, fluid viscosity and particle size (see next section). We will refer hereafter to ζ as a compaction or consolidation viscosity.

After some algebra (supplements) we arrive at a two-phase description of the physics for hindered settling

$$\frac{\partial X}{\partial t} = -\frac{\partial [\mathrm{X}\, V_s]}{\partial z}, \quad (11)$$

$$\frac{\partial}{\partial z}\left[(1-X)V_f + \mathrm{X}\, V_s\right] = 0, \quad (12)$$

$$\frac{c}{1-X}\left(V_f - V_s\right) + \mathrm{X}\, \Delta\rho g + \frac{\partial}{\partial z}\left[X\, \zeta \frac{\partial V_s}{\partial z}\right] = 0. \quad (13)$$

The momentum conservation equation contains a characteristic length scale

$$\delta = \sqrt{\frac{\zeta (1-X)^2}{c}} = \sqrt{\frac{\zeta}{\beta}} \quad (14)$$

where $\beta = c/(1-X)^2$ . The length scale $\delta$ serves as a compaction length in this model. The compaction length in a highly viscous compacting matrix with relatively small fluid fractions (e.g. melt migration) is discussed by McKenzie (1984). The physical process here might be better called consolidation rather than compaction, but we retain the use of compaction length since this is a familiar term.

## 2.2. Closure model for the interphase drag: Hindered settling velocity

The closure of the two-phase continuum description for settling requires a model for the interphase drag coefficient *c* in the governing equations (e.g. Eq. 13). Assuming that the solid phase does not deform ($\mu_s \to \infty$) the drag coefficient is expected to depend on the particle shape and size (*a*), the fluid viscosity, $\mu_f$, and the particle volume fraction, *X*.

We determine this coefficient using the limit where the particle volume fraction field *X* is homogeneous ($X \neq X(z)$) and the compaction term in the momentum conservation vanishes (because $\frac{\partial V_s}{\partial z} \to 0$). Under these idealized conditions, the momentum conservation can be further simplified by recognizing that the average separation velocity between the two phases is given by the uncorrected hindered settling velocity, $V_H$,

$$\frac{c}{1-X}\left(V_f - V_s\right) + X\, \Delta\rho g = -\frac{c}{1-X} V_H + X\, \Delta\rho g = 0 \quad (15)$$

where $V_H$=$V_s$-$V_f$ is the uncorrected hindered settling velocity. This can be further expanded to

$$\frac{c}{1-X} V_{Stokes}\, H(X) = \mathrm{X}\, \Delta\rho g \tag{16}$$

where

$$V_{Stokes} = \frac{2\Delta\rho g a^2}{9\,\mu_f} \tag{17}$$

for solid spherical particles. Therefore, the drag coefficient, *c*, can be determined from empirical hindered settling laws in homogeneous suspensions and yields

$$c = \frac{9\mu_f}{2a^2}\frac{X(1-X)}{H(X)}. \tag{18}$$

The drag coefficient can alternatively be expressed as a "settling permeability"

$$K_{settling} = \frac{2a^2 H(X)}{9X}. \tag{19}$$

A number of empirical expressions for the hindrance function, $H(x)$, relating normalized settling velocity and solid volume fraction have been published (see Davis and Acrivos, 1985). While most reproduce experimental data well at low solid fractions, their applicability to high solid volume fraction values is more ambiguous. For instance, while the parameterizations of Richardson and Zaki (1954) and Faroughi and Huber (2015) agree generally well at low volume fraction, the latter vanishes at a maximum packing fraction $X_m$ while the former does not. We argue here that a proper parameterization for hindrance should retrieve familiar parameterizations of flow through a permeable, non-deformable medium at solid fraction near or in excess of the maximum packing. We construct a hindrance function parameterization that matches predictions from porous flow (Kozeny-Carman permeability parameterization) at high solid fraction and matches the hindrance parameterization of Faroughi and Huber (2015) at low to moderate particle fraction. This parameterization is given by Eq. (20a)

$$H(X) = \frac{A(1-X)^2}{A+10X^2} \quad \text{with } A\text{= 0.4 the relationship adopted here} \tag{20a}$$

and compared to the parameterization of Richardson and Zaki (1954)

$$H(X) = (1-X)^{4.65}, \quad \text{Richardson and Zaki (1954) for low } X \tag{20b}$$

and a hindrance function computed directly from the Kozeny-Carman permeability parameterization

$$H(X) = \frac{(1-X)^2}{40X^2}, \ \text{Kozeny–Carman permeability for } X \text{ approaching } Xm \tag{20c}$$

all plotted together in Fig. 1a.

Written in terms of the hindered settling function, the mass conservation of solid reads

$$\frac{\partial X}{\partial t} = -\frac{\partial}{\partial z}[V_s\, X] = -\frac{\partial}{\partial z}[V_{stokes} H(X) X(1-X)] = -\frac{\partial F_X}{\partial z} \tag{21}$$

where $V_s = (1-X)H(X)V_{Stokes}$ and $F_X = V_{stokes} H(X) X(1-X)$. Here, $F_X$ is the particle flux at depth, z. The particle flux as defined here is only a function of the particle solid fraction, *X*, and therefore

$$\frac{\partial X}{\partial t} = -V\frac{\partial X}{\partial z} \tag{22}$$

which describes a kinematic wave for the solid volume fraction with speed $V = \frac{\partial F_X}{\partial X}$. Hindrance functions, particle flux and kinematic wave speeds obtained using 20a are shown in Figure 1.

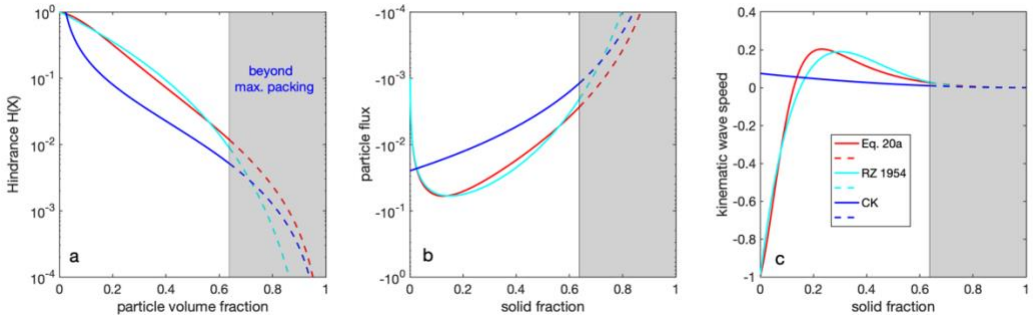


Figure 1. Illustration of the different closure models for the particle hindrance, particle flux and kinematic wave speed. Panel a compares the settling model we propose in Eq. 20a to the Richardson and Zaki (1954) empirical model (Eq. 20b) and a Kozeny–Carman model (Eq. 20c) for high particle volume fraction. Panel b shows the particle flux as function of solid fraction for the same laws as in panel a. Panel c shows the derivative of particle flux, $F$, with respect to solid fraction, which is defined as the kinematic wave velocity for each of the same three models. The particle flux, and kinematic wave velocity are negative because we take gravity to be directed along the negative z-direction.

## 2.3. Closure models for the compaction viscosity with solid particles

The corrected version of hindered settling that we propose requires a definition for the compaction viscosity ζ to provide closure to the continuum conservation equations (11, 12, and 13). Intuitively, the compaction or consolidation viscosity must depend on the solid fraction (or conversely the porosity), the size/mode of particles and on the fluid viscosity $\mu_f$. It shares the same dimension and should be proportional to the fluid viscosity. Another important note here is that the compaction viscosity, ζ, should vanish at small particle volume fractions.

In this section, we discuss models to provide a closure to the compaction viscosity from first principles using two general limits of solid fraction. The first model is based on the concept of point forces in Stokes flow and provides a guide for the dependence of the compaction viscosity on porosity in the limit of low particle volume fraction. The two other models provide alternatives at high particle volume fraction, as the volume fraction approaches jamming conditions.

Before discussing these closure models in detail, it is important to build a conceptual understanding of how the forces that act on the particles are affected by changes in solid fraction. As an illustration, we use the simple geometrical model shown in Figures 2. This highly idealized geometry is particularly useful in distinguishing viscous dissipation associated with consolidation/compaction from that for pure hindered settling. In panel X, blocks move with a uniform vertical velocity corresponding to hindered settling alone. In panel X, particles that settle with a vertically varying velocity. Hindered settling with compaction is described by the superposition of the two.

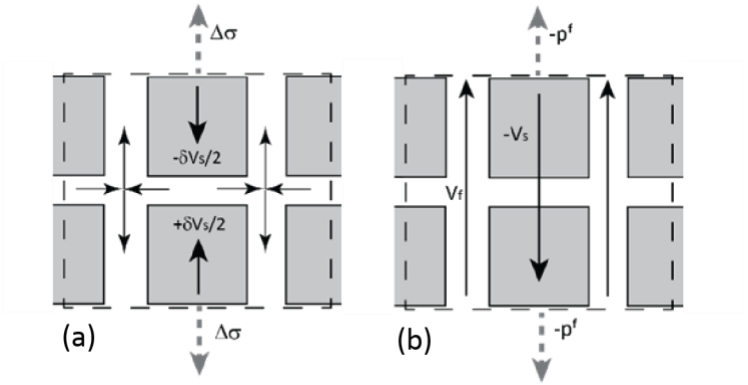


Figure 2. Idealization illustrating the viscous flow imposed by compacting (or consolidating) and settling in suspensions. On the right, all particles settle vertically with a uniform velocity $V_s$ (REV shown by the dashed lines) balanced by an opposing vertical flow between the particles $V_f$. The hindered settling velocity $V_s - V_f$ is determined by a balance between gravitational forces and the viscous dissipation of vertical flow between the particles. This is contrasted with the scenario on the left where the solid fraction decreases (particles get closer) because of a local perturbation in solid velocity $\delta V_s$. Additional viscous dissipation is caused by fluid being expelled from closing spaces between particles.

As shown in the following section, we find that the topology of the domain influences the definition of the compaction viscosity but that there are some common characteristics that can be used to develop a generic (idealized) closure model.

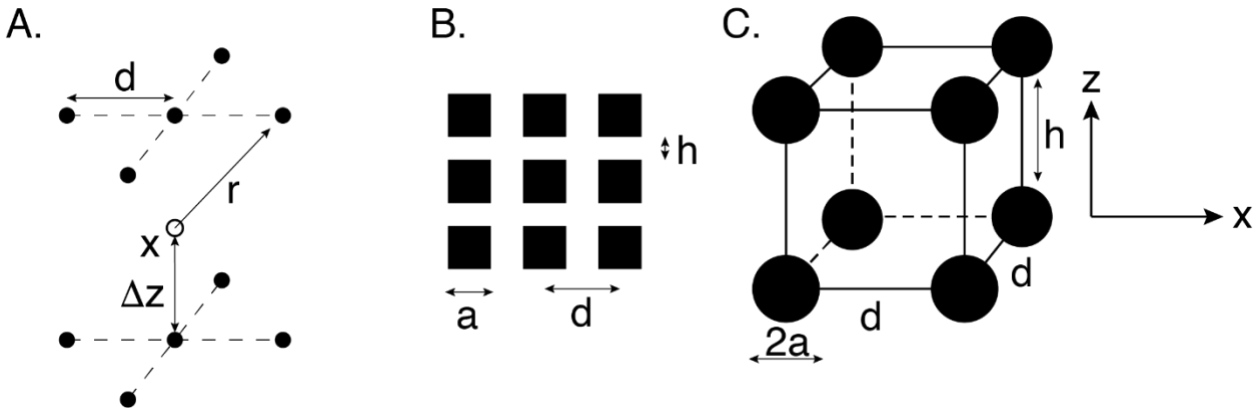

Figure 3. Geometrical models for the closure relationship between compaction viscosity and porosity. (A) shows the 10 nearest neighbors model used for the limit of high porosity, x is the observation point. (B) 2-D square model used for the limit of low porosity compaction viscosity and (C) with a simple cubic lattice.

**Compaction viscosity at low solid fraction**

At low solid fraction, solid particles are far apart, i.e. if the particle size is *a* and the interparticle (nearest neighbor distance) is *d*, then *a/d* << 1 and the particle shape does not affect the flow in the far-field. This limit allows for some useful simplifications. Most importantly it is possible to consider that particles act as point forces on the fluid.

The pressure perturbation caused by a point force on the fluid at position *x* in a homogeneous background flow with velocity $V_p$ is (Batchelor, 1970; Guazzelli and Morris, 2012)

$$\tilde{p} = \frac{3}{2}\mu_f \, a \frac{\overrightarrow{V_p}\cdot\vec{x}}{r^3} \tag{23}$$

where *r* is the distance between the particle (point force) and the observation point in the fluid, $\vec{x}$, and $\mu_f$ is the fluid viscosity (see Figures 3 panel A). We now consider particles spaced far apart on a simple cubic lattice and a smoothly spatially varying average separation velocity between the fluid and the particles (non-homogeneous) such that

$$V_{p,z}(z) \cong V_{p,z}(z_0) + \frac{\partial V_{p,z}}{\partial z}\Delta z, \tag{24}$$

where $\Delta z = z - z_0$ and $z_0$ is a point in the fluid centered between two layers of particles in the lattice. The nearest 10 neighbors each contribute to the pressure perturbation to yield

$$\tilde{p} = \frac{3}{2}\mu_f \, a \left[\sum_{i=1}^{5} -\frac{\partial V_{p,z}}{\partial z}\frac{\Delta z^2}{r_i^3} + \sum_{i=1}^{5} -\frac{\partial V_{p,z}}{\partial z}\frac{(-\Delta z)^2}{r_i^3}\right]. \tag{25}$$

The two terms on the right-hand side are the contribution to pressure caused by the particle above and below the reference position $\vec{x}$. With the configuration shown in Fig. 3a, the particle volume fraction is expressed as

$$X = \frac{4\pi a^3}{3\Delta z^3} \tag{26}$$

and, from equation 10, we get the compaction pressure (identifying the solid fraction velocity $V_s$ to the continuum-scale particle velocity $V_p$)

$$\Delta\sigma = \tilde{p} = \frac{3}{2}\mu_f \left(2 + \left(\sqrt{2}\right)^3\right)\left(\frac{3}{4\pi}\right)^{1/3} \mathrm{X}^{1/3}\frac{\partial V_s}{\partial z}. \tag{27}$$

This allows us to define, in this regime of low solid fraction, the compaction viscosity

$$\zeta = \frac{3}{2}\mu_f \left(2 + \left(\sqrt{2}\right)^3\right)\left(\frac{3}{4\pi}\right)^{1/3} \mathrm{X}^{1/3} \tag{28}$$

which vanishes in the limit of X → 0 as expected. The geometric factors in the compaction viscosity are a result of the arbitrary topology of the periodic arrangement of particles which are roughly of order unity. Here, $\zeta$ exhibits a linear dependence with respect to the fluid viscosity (as expected in the Stokes flow regime) and a cubic root dependence with respect to the particle volume fraction.

**Compaction viscosity at high solid fractions (approaching particle-particle contact)**

The first closure model that we explore for the limit of high solid fraction is based on a two-dimensional periodic lattice of squares (see Figures 3, panel B). Assuming again that the continuum approximation for the particle velocity is a smoothly varying function of the vertical position z and given the definitions in Figures 3b, Δz=a+h is the vertical distance between neighbor particle centers, and h is the gap between the particles. By definition, the change of gap thickness over time is

$$\frac{dh}{dt} = -\frac{\partial V_{p,z}}{\partial z}\Delta z = (a+h)\frac{\partial V_{p,z}}{\partial z}. \quad (29)$$

Using mass conservation of fluid in the gap

$$\frac{a}{2}\frac{dh}{dt} = -\langle V_{f,x}\rangle h, \quad (30)$$

and defining the vertically averaged fluid velocity in the gap $\langle V_{f,x}\rangle$

$$\langle V_{f,x}\rangle = -\frac{h^2}{12\mu_f}\frac{\partial \Delta P_f}{\partial x}, \quad (31)$$

and the pressure drop can be approximated by

$$\frac{\partial \Delta P_f}{\partial x} \cong \frac{\Delta P_f}{\frac{a}{2}}. \quad (32)$$

Again, identifying the continuum $V_p$ with the solid fraction velocity Vs allows us to retrieve an expression for the pressure perturbation caused by the heterogeneous solid fraction velocity field

$$\Delta\sigma = \Delta P_f = 3a^2\frac{(a+h)}{h^3}\mu_f\frac{\partial V_s}{\partial z}. \quad (33)$$

Defining the particle volume fraction as

$$X(h) = \frac{a^2}{(a+L)(a+h)}, \quad (34)$$

the compaction viscosity can be defined with respect to the particle volume fraction and a maximum particle volume fraction ($\mathrm{X}_m = X(h\to 0) = 1-\frac{L}{a+L}$)

$$\zeta = 3\mu_f \mathrm{X}_m \frac{X^2}{(X_m - X)^3}. \quad (35)$$

As expected the compaction viscosity is proportional to the fluid depends linearly on the fluid's viscosity but has a different dependence (stronger) on particle fraction and diverges as the porosity approaches the residual porosity (no more vertical space to accommodate compaction).

Simple cubic lattice of spherical particles

An alternative model can be derived for a simple cubic lattice of spherical particles. In this model, with definition of the particle spacing illustrated in Figure 3c, the particle volume fraction is

$$X = \frac{4\pi a^3}{3d^2(a+h)}. \tag{36}$$

Assuming that the gap between particles h << a in the limit of porosity approaching the jamming conditions (vertically), then we can use a lubrication approximation to use the same argument as for the two-dimensional array of squares for the mass conservation

$$\frac{a}{2}\frac{dh}{dt} = -\langle V_{f,x}\rangle h, \tag{37}$$

and using the average fluid velocity-pressure relationship obtained theoretically (and validated numerically) by Zick and Homsy (1982)

$$\frac{\Delta P_f}{a/2} = -\frac{9}{2}\frac{\mu_f}{a^2}\mathrm{c}_{ZH}\ K\langle V_{f,x}\rangle, \tag{38}$$

with $c_{ZH}$ a drag correction computed for a periodic array of spheres in Zick and Homsy (1982) that is approximated by

$$\mathrm{c}_{ZH} \cong \frac{10\,\mathrm{X}}{(1-X)^3}. \tag{39}$$

With a maximum particle volume fraction

$$X_m = \frac{4\pi a^2}{3d^2}, \tag{40}$$

we get the compaction viscosity

$$\zeta = \frac{45}{4}\mu_f \frac{\mathrm{X}_m X^2}{(\mathrm{X}_m - X)(1-X)^3}, \tag{41}$$

which diverges, as expected, when the particle volume fraction approaches $\mathrm{X}_m$.

The compaction viscosity and the associated compaction length as function of the solid fraction for the model with spherical particles (Eq. 41) is shown in Figure 4. One notes that the compaction viscosity and therefore the compaction length are negligible at low solid fraction and mostly matter near the maximum packing fraction.

It is interesting to note that the singularity as $X \rightarrow \mathrm{X}_m$ is much stronger in the simple cube model, $(\mathrm{X}_m - X)^{-3}$ rather than $(\mathrm{X}_m - X)^{-1}$ for spherical particles. This suggests, not surprisingly, that grain shape as well as grain size are likely to be important to the behaviors that we describe below.

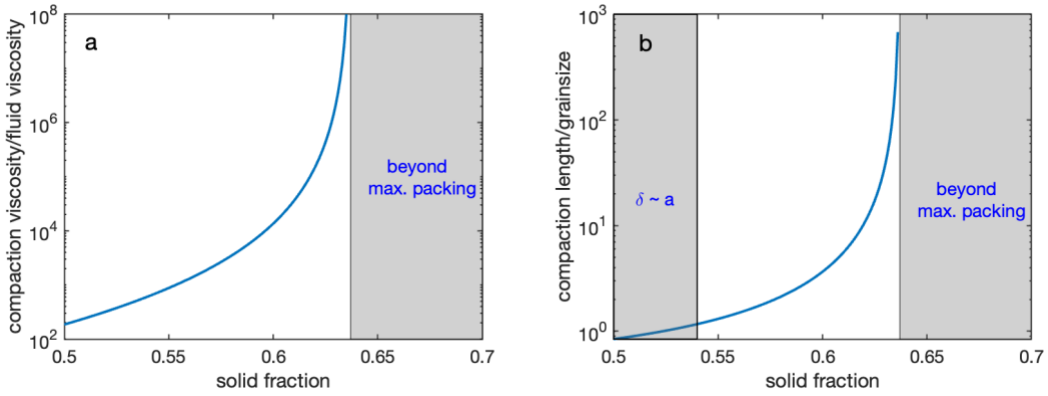


Figure 4. (a) Dependence of the compaction viscosity on the particle volume fraction, using the model in equation (36). (b) Effective compaction length (normalized by particle size) as function of the particle volume fraction for the same compaction viscosity as in the left panel.

## 3. Results

We conduct a series of numerical experiments to explore the behavior of settling with and without compaction viscosity. Formulation of numerical methods applied to equations (11-13) are summarized in Appendix 1; nondimensionalization of the equations is summarized in Appendix 2. First, we consider a settling front in an infinite domain, and specifically the effect of the compaction viscosity on the development of front instabilities and structure. Second, we consider settling adjacent to a solid boundary and the effect of a compaction viscosity on the formation and growth of a cumulate layer above that boundary.

### 3.1 Stability and structure of a sedimentation front

To examine the role of compaction viscosity on the structure of a sedimentation front, we consider the evolution of an initial depth distribution having the form of an error function with solid fraction increasing both upward and downward. A layer with crystal fraction increasing upward might form, for example, at the top of a mushy igneous intrusion where cooling of the crystal-melt suspension at the top results in a upward increase in crystallinity. At large scales similar behavior may be present in magma oceans which solidify by cooling at the planetary surface. Solid fraction increasing downward could correspond with regions near the bottom of a convecting magma ocean. Our objective here is not to consider either of these environments in detail, but to examine suspension dynamics that could help better understand processes occurring there.

These examples on an infinite domain assume a vanishing gradient in solid fraction at both the top and bottom implying that particles on the boundary settle at the hindered settling velocity. The reference frame in these infinite domains is defined by setting the fluid velocity to vanish at the lower boundary and therefore in the whole halfspace below the evolving front structure. Height along the vertical z coordinate is normalized by the reference compaction length. The settling direction is along the negative z-axis corresponding to a downward direction for gravity and velocity for particles that are denser than the fluid.

We first consider a simplified case where the compaction viscosity $\zeta$ is constant ($= \zeta_{ref}$). This is followed by a more general case where the compaction viscosity depends on the local particle volume fraction as inferred in section 2.2. As discussed above the compaction viscosity and corresponding compaction length are small for solid fractions well below the closest packed solid fraction $X_m$. At these low volume fractions the compaction length is expected to be comparable to the particle size (see Figure 4b). Under these conditions using a continuum approximation to describe the compaction behavior is inappropriate, thus we explore cases with high particle volume fraction near $X_m$.

**Constant compaction viscosity**

The evolution of a sedimentation front is controlled by both the compaction viscosity and the variation of the kinematic wave speed with solid volume fraction shown in Figure 1. Since the effects of compaction viscosity are most important at high solid volume fractions, we consider an initial solid fraction varying from 0.4 to 0.6 with a width of 2 reference compaction lengths. This range of solid fractions is above the kinematic wave speed maximum; the kinematic wave speed decreases with increasing solid volume fraction. Starting with the case shown in Figure 5a with solid fraction increasing in the settling direction (downward), particles in the low solid fraction region settle more rapidly than those in the higher solid fraction region beneath onto which settling particles accumulate. The front widens as it propagates upward into the region of lower solid fraction. If the initial front is approximated by small discontinuous steps in solid fraction, the lower magnitude of the wave speed at larger volume fractions (see inset in 5b and Figure 1 where a negative speed means a propagation direction opposite to settling) causes these parts of the front to be left behind so the front continuously broadens with time. Horizontal lines In Figure 5 mark the location of the finite amplitude kinematic wave front (see Figure 1 and discussion above) at each time shown.

With solid fraction decreasing in the settling direction, shown in Figure 5b, the opposite behavior occurs. Particles at depth settle more rapidly than those in higher solid fraction regions above. The higher kinematic wave speed magnitude at smaller particle volume fractions causes small steps of decreasing particle volume fraction to accumulate ahead of the steepening front. In the absence of a compaction viscosity, the front, as it propagates to

shallower depths, would steepen to a discontinuity that propagates at the kinematic wave speed for a front of this amplitude. As in Figure 5a, horizontal lines mark the location of the finite amplitude kinematic wave front at each time shown. With a nonzero compaction viscosity, the initial front first steepens; but after reaching a width comparable to a few compaction lengths, a system of trailing waves develops. This nearly harmonic-like wave train, with a wavelength of several local compaction lengths, is initiated as the solid fraction at the steepened front undershoots that behind the upward moving front. The wave behavior is a consequence of the phase shift between compaction stresses and compaction rate implied in the above discussion (equation 13). The front with nonzero compaction viscosity propagates at a slightly slower speed than a purely kinematic discontinuous front of the same amplitude reflecting the dissipation rate in the trailing wave train. Viscous dissipation also causes the wave train to decay with distance behind the upward moving front.

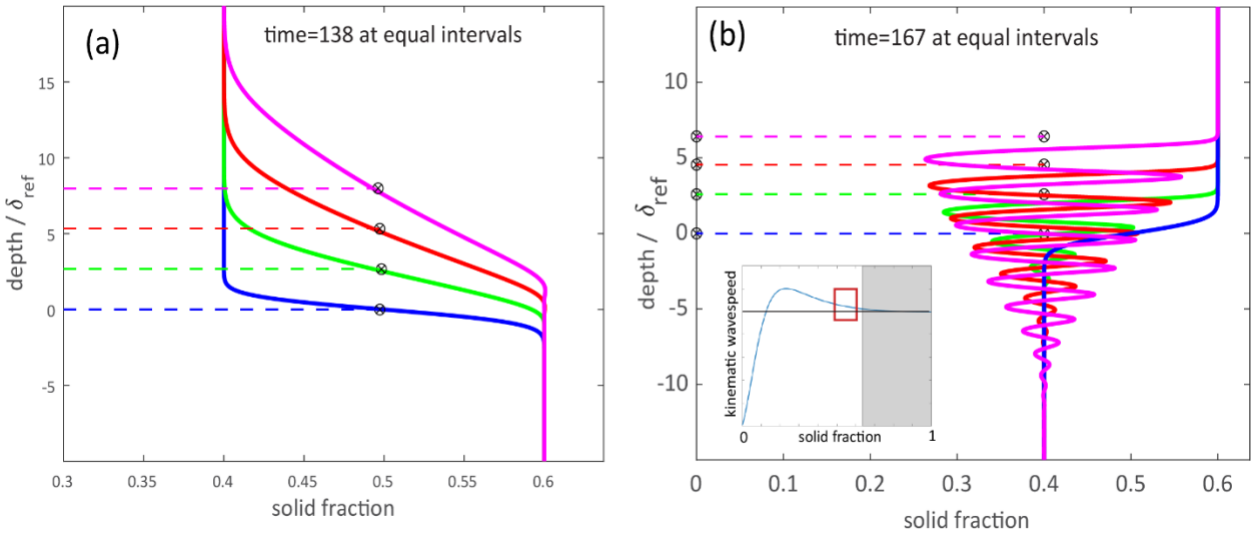


Figure 5. Evolution of an initial depth distribution of solid fraction with the form of an error function varying between 0.4 and 0.6 with a width of 2 reference compaction lengths. Colors blue through purple show the structure of the front at progressively longer times. (a) initial solid fraction increasing in particle settling direction (downward). Dashed horizontal lines at each time show the calculated location of a discontinuous front of this amplitude propagating at its kinematic wave speed. (b) solid fraction decreasing in the settling direction (downward).

This dispersive front behavior has also been described in numerical solutions for melt migration (small fluid fractions in a continuous high viscosity matrix) by Spiegelman (1993). A more recent detailed analysis of this behavior relevant to the rise of a buoyant fluid in a viscously deformable conduit or melt migration is discussed by Lowman and Hoeffer (2013). The behavior that we see here for particle consolidation at high solid fractions mimics the results reported in these earlier studies. The analytical framework proposed in these previous studies should be helpful in a more detailed study of the behavior described here and in the following section.

## Compaction viscosity varying with solid fraction

As shown in Figure 6, a depleted (in terms of solid fraction) layer develops with a compaction viscosity that increases rapidly with increasing particle volume fraction, as $X$ approaches $X_m$ (see Figure 4). The relatively uniform, depleted layer is bounded by two fronts as shown in Figure 6, but is most clearly developed in Figure 6b. These fronts include the initial front, as well as a second front that emerges with a particle density that increases in the settling direction. For the two cases shown the layer thickens more rapidly for the case with a greater contrast in solid fraction at the initial front. The lower layer progressively thickens while the solid fraction within the depleted layer remains nearly constant. The solid fraction within the depleted layer has nearly the same value for the two fronts of differing amplitude shown in panels a and b in Figure 6.

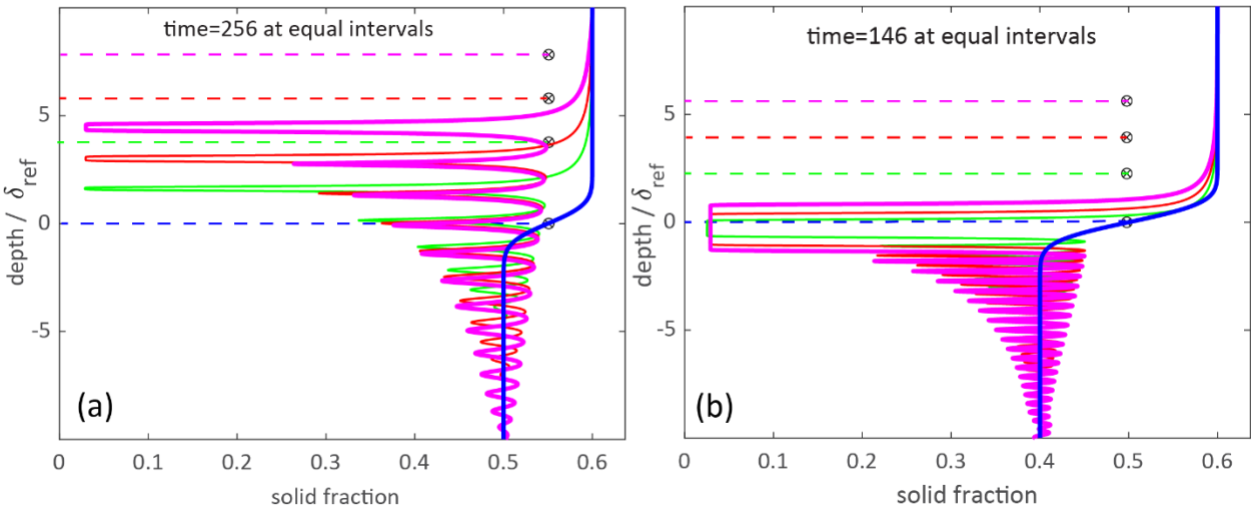


Figure 6. Evolution of an initial depth distribution of solid fraction with the form of an error function varying from 0.5 to 0.6 (panel a) and 0.4 to 0.6 (panel b) with the same width as in Figure 4 but with a compaction viscosity that increases strongly as solid fraction approaches the closest packed solid fraction (0.637 in this example). Compaction viscosity varies with solid fraction as shown in Figure 1 and equation (42). As in Fig. 5 dashed horizontal lines show the calculated location of a discontinuous front propagating at the kinematic wave speed at each time. Note the reduced speed of the propagating front compared to the kinematic wave speed.

## Development of depleted layer

The development of the depleted layer is intuitively reasonable since the particle flux for smaller solid fractions beneath the initial front is higher than at the larger solid fraction above it, creating the low solid fraction region between the fronts. However, understanding the structure of the two fronts and the development of a liquid-rich layer requires further study. The variation of kinematic wave speed with solid fraction (Figure 1) and the variation of compaction length and viscosity (Figure 4) may both play a role. Wave speed variation alone can result in

interesting behavior of kinematic front evolution (cf. Kynch 1952; Fitch 1983), but with a constant compaction viscosity (Figure 5) the variation of wave speed alone does not show the formation of a depleted layer. Furthermore, an initially prescribed, low solid fraction layer defined by kinematic fronts (vanishing compaction viscosity)does not persist with time as shown in Figure 7b. Thus, the variation of compaction viscosity with solid fraction appears to be an essential component of this behavior.

As shown in Figure 7a, the early evolution of the initial front (blue) is reminiscent of that seen above in Figure 5b, consisting of a damped wave train developing behind a steeping front. As the trailing wave train amplitude increases with time the layer emerges as the solid fraction decreases to values at which the compaction length is negligibly small. Note also that the behavior of this trailing front is the opposite of that seen with constant compaction viscosity (Figure 5) where the steepening of a front occurs only as the solid fraction increases in the propagation direction.

Figure 7 (b) shows the behavior of a kinematic front initially containing a depleted (low solid fraction) layer like that in Figure 6, but considering a case where the compaction viscosity is vanishingly small and constant. Here, since the reference compaction length is negligible, the vertical scale is normalized by the initial width of the layer. In the absence of a compaction viscosity, both the thickness and amplitude of an initially prescribed low solid fraction layer decays with time as the two kinematic fronts interact as shown here, again demonstrating the fundamental role of compaction viscosity in the behavior seen in Figure 6.

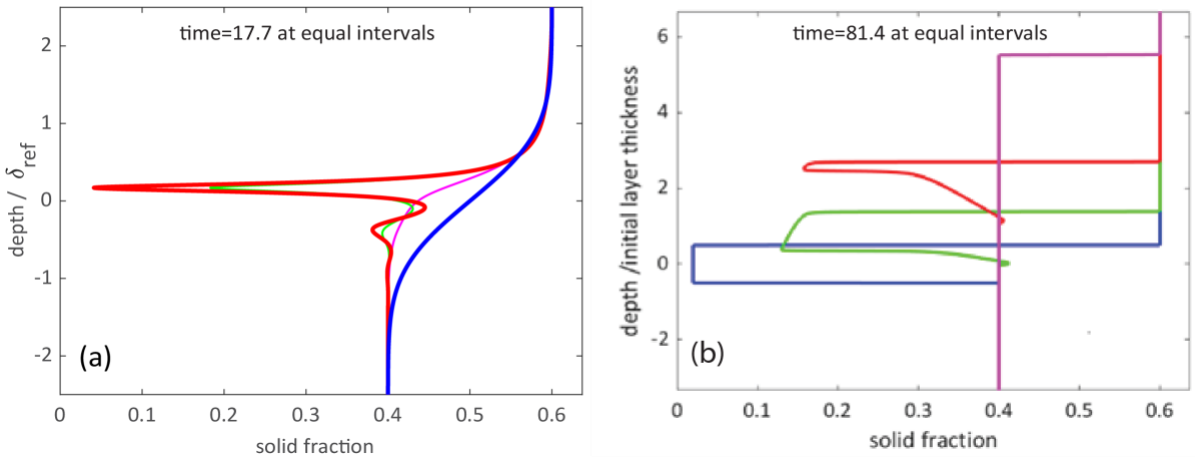


Figure 7. (a) Early stages in development of the low solid fraction layer shown over longer times in Figure 6b. The layer develops as growing waves (purple, green, then red) behind the initial front (blue) reach a low solid fraction where the compaction length is small. The compaction viscosity variation with solid fraction is that same as in Figure 6, with large values near $X = X_m$ and small vanishing small values for small $X$. As before horizontal lines denote the location of the kinematic wave front at each corresponding time. Note that the dissipative waves along with the development of the layer reduces the upward velocity of the settling front. (b) Evolution of initially prescribed low solid fraction layer for vanishing compaction viscosity. Note that the initially imposed layer does not

519 persist with time. The depth coordinate in this example with vanishing compaction length is
520 normalized by the initial low solid fraction layer thickness.

521 One potentially important consequence of the development of a low solid fraction layer may be
522 the buoyant Rayleigh-Taylor (RT) instability of such a low density, low viscosity layer (Whitehead
523 1988; Wilcox and Whitehead, 1991; Lister and Kerr, 1989). The bulk viscosity in the depleted
524 layer may be 4 to 6 orders of magnitude smaller (cf. Costa et al 2009, Faroughi and Huber, 2023)
525 than in the higher particle fraction suspension above and below it. Since the wavelength of the
526 fastest growing RT instability is proportional to the cube root of this viscosity ratio, the low
527 viscosity of the layer can be expected to promote a long wavelength instability leading to phase
528 segregation on a scale that should be several orders of magnitude greater than the layer
529 thickness. Instability growth rate also increases with the layer thickness. Our numerical
530 experiments suggest that the growth rate of the layer is nearly constant with time, whereas the
531 growth rate of the RT instability will increase linearly with the layer thickness. Thus, when the
532 layer thickness is large enough, the growth rate of RT instability should exceed the growth rate
533 of the layer thickness so that we expect that RT instability can eventually control the dynamics
534 of the layered suspension. The low viscosity in the layer should also promote incipient
535 convective instability of the denser suspension above and below it.

536 **3.2 Growth of a cumulate layer by hindered settling**

537 The effect of the compaction viscosity correction on hindered settling is clearly visible in the
538 structure of a growing cumulate layer above a solid (no flux) bottom boundary shown in Figure
539 8. Both the layer thickness and trapped melt distribution are drastically different when the
540 effect of compaction/consolidation is included. The effective settling velocity versus solid
541 fraction departs from the hindrance function only at high solid fraction with the compaction
542 correction, which is not surprising given the fact that the compaction viscosity and compaction
543 length are significantly greater for these values (Figures 3), which amplifies the relative
544 contribution of the compaction term in the momentum conservation equation. At high solid
545 fraction the settling velocity vanishes at $X_m$ because it marks the limit where compaction by
546 settling is no longer possible as the suspension reached its maximum packing fraction. Without
547 the compaction term, settling is controlled solely by the hindrance function which continuously
548 and monotonously decreases to 0 when the solid fraction reaches 1. In the absence of a
549 compaction term in the momentum conservation, the cumulate layer can reach a solid fraction
550 of 1, well beyond the maximum packing of the solid particle suspension. This is unphysical
551 because there is no prescribed compaction model to consider consolidation past the maximum
552 packing here. In contrast, the consideration of the compaction term in the momentum
553 conservation limits the maximum solid fraction to the prescribed maximum packing value, a
554 suspension under settling alone cannot reach a solid fraction beyond the maximum packing.
555 The curvature of the solid fraction depth profiles differs significantly when the solid fraction of
556 exceeds about 0.5 in this example. The profile is concave without compaction, while it is convex
557 and pinned to the maximum packing fraction otherwise. The degree of curvature depends on

the effective compaction length with depth over the lower section, a greater compaction length leading to a lower maximum curvature while a smaller compaction length would generate a more step-like transition from the cumulate layer to the settling suspension.

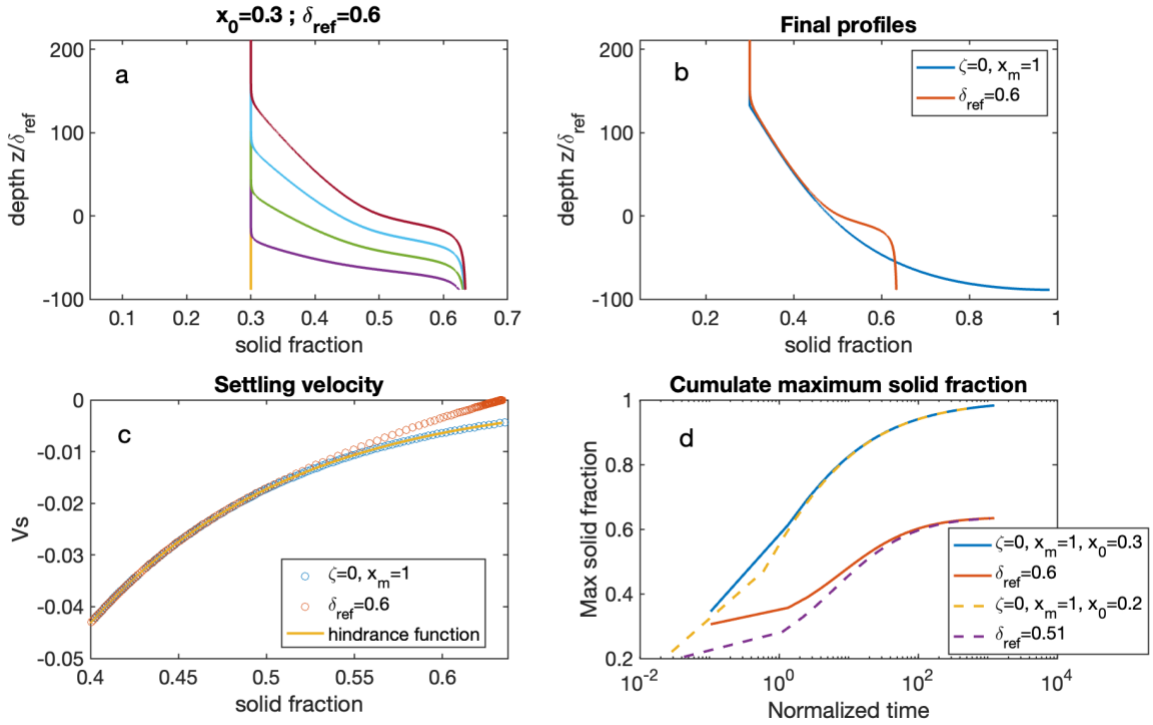


Figure 8. (a) Solid fraction that accumulates in a layer adjacent to a solid (no flux) boundary beneath a halfspace in which the initial solid fraction has the uniform values 0.3, this case includes a solid fraction dependent compaction viscosity. (b) Comparison of solid fraction distribution with (red) and without (blue) the effect of compaction viscosity on hindered settling. The blue curve compares the solid fraction without compaction viscosity with the final time in (a). (c) Deviation of local settling velocity (red circles) from that predicted by the hindered settling function without compaction viscosity (blue line). (d) Evolution of the maximum solid fraction in the cumulate over time for 4 simulations, the blue and red lines show the case with a starting homogeneous solid fraction of 0.3 and with and without compaction respectively and the orange and purple dashed lines show the case a starting homogeneous solid fraction of 0.2 with and without compaction.

The lower right panel of Figure 8 shows the maximum solid fraction in the profile as function of time considering four different cases. Here runs with an initial solid fraction of 0.2 and 0.3 are compared to equivalent runs where the compaction viscosity was set to 0 (uncorrected hindered settling). As expected it takes more time to build the cumulate layer to the same maximum solid fraction starting from a lower solid fraction, and unsurprisingly with time the starting solid fraction does not impact the maximum solid fraction reached in the simulation. The major control over the maximum solid fraction in the cumulate layer is whether one accounts for a finite compaction viscosity or not.

## 4. Discussion: implications of the new settling model

The main purpose of this study has been to introduce the effect of compaction/consolidation viscosity in sedimentation. Hindered settling velocity describes the settling velocity accounting for interaction between particles with a *spatially uniform* particle density. Viscous dissipation due to particle settling is reflected in the reduced settling velocity relative to an isolated particle. In a continuum description, a spatial and/or temporal variation of the particle volume fraction in an REV introduces viscous dissipation in addition to that due to particle settling alone. We illustrate this with several simple or idealized examples. We show that this additional viscous dissipation rate can be expressed by a product of compaction or consolidation viscosity with the material derivative of the particle volume fraction describing the additional local average force acting on particles. We also provide some simple models to estimate the magnitude of the compaction viscosity, which is particularly large as the solid fraction increases toward the jamming condition.

We see important consequences for the sedimentation front structure behavior. Variation of the hindered settling velocity with solid fraction has an important influence on the evolution of a settling front. An initially smooth front widens or narrows with time depending on whether the particle flux increases or decreases in the settling direction (e.g. Guazzelli and Morris, 2012; Kynch 1952). A narrowing front described solely by the variation of the hindered settling velocity with particle volume fraction steepens to form a nonphysical discontinuity.

With compaction viscosity present, we find that the front propagates at a slower speed than a discontinuous kinematic front. Dissipation associated with compaction viscosity limits how sharp the front can become, that is how rapidly the REV can gain or lose solid particles. Our results show a train of harmonic-like waves develops behind the front with an amplitude that decays with distance behind the front. The wavelength of the wave train and the distance over which it decays scales directly with the compaction length behind the front.

The combined effects of the variation of hindered settling velocity with solid volume fraction and the presence of a compaction viscosity lead to the prediction of complex behavior in the structure of a sedimentation front. An initial front can breakdown into a complex structure that allows the formation of layers with very low solid fraction.

Recently, Lee and Morton (2015) argued that hindered settling plays a key role in the separation of high silica melts from their crystal cargoes necessary to the formation of high silica granites (HSG). The arguments that favor hindered settling are (1) the range of estimated residual melt fraction in the left-over cumulates overlaps with values inferred for maximum packing and (2) the timescales of separation by hindered settling, unlike those of more melt-depleted compaction processes, are shorter or comparable to the cooling timescales of the host magma body. In a parallel study, Lee et al., compute these settling timescales from hindered settling laws based on the empirical correlation of Richardson and Zaki (1954). As a comparison, we recomputed their analysis using the same framework to calculate the time it takes to clear a

suspension of a given solid fraction *X* (or alternatively porosity 1-*X*) over a thickness of 25 meters (see Figure 9). The solid line is identical to that calculated in Lee et al. (2015), the line with circle symbols is computed from the hindered settling function we use in this paper (Eq. 20a) and finally, the two trends with cross symbols shows actual solutions of our corrected hindered settling model used to generate Figures 8C which accounts for the dissipation of energy caused by changes in solid fraction, the yellow trend for the random maximum packing for monodisperse spheres (phi=0.37) and the purple trend for the maximum close packing of spheres (phi=0.26). Unlike the other two curves, the corrected model diverges at the maximum packing fraction. It also shows that hindered settling times are generally longer, especially as the solid fraction increase, than what is generally inferred from other models. Importantly, unlike other models, it predicts that hindered settling cannot reduce porosity beyond the maximum packing and that other, likely less efficient, processes are required to further compact a cumulate. This again is consistent with the lowest trapped melt fraction estimated from geochemistry being estimated around what is expected from maximum packing (Lee and Morton, 2015).

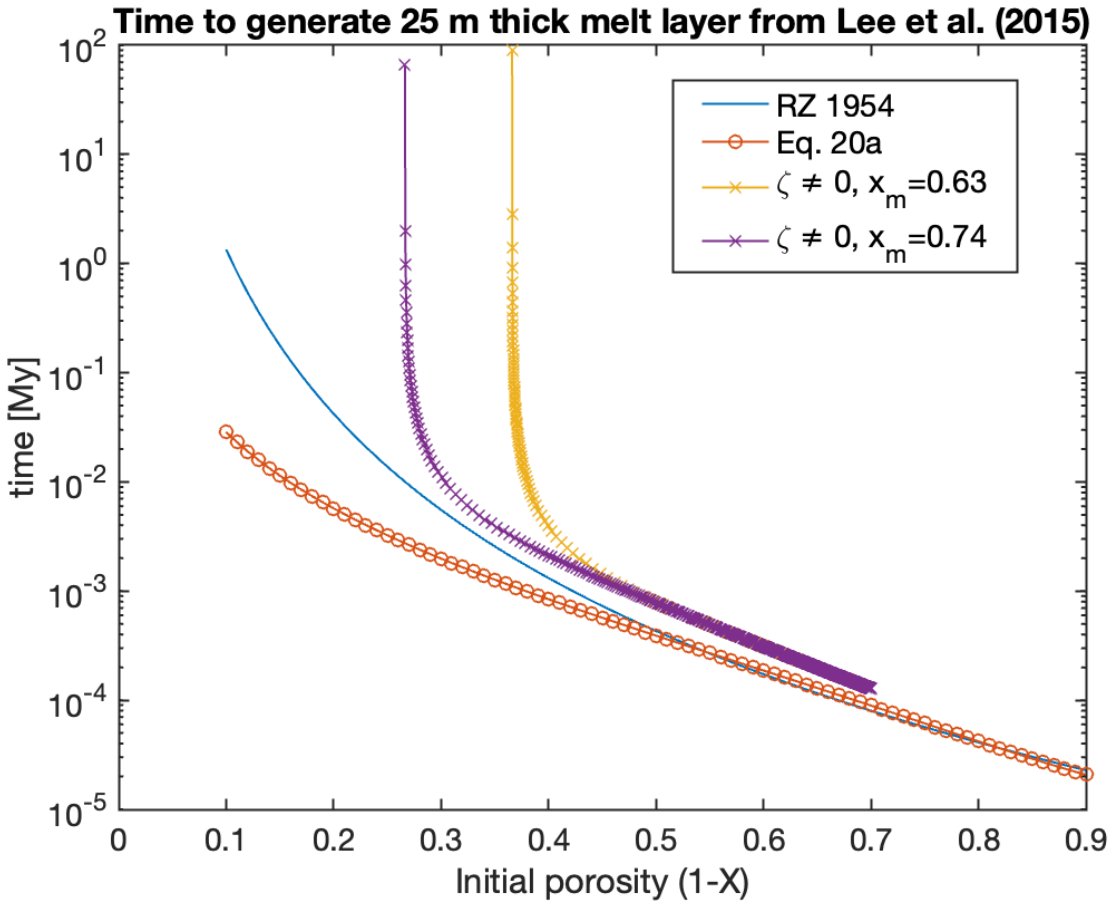


Figure 9. Estimated time to clear a suspension with a given initial porosity over a layer of 25 meters of thickness assuming a melt viscosity of $10^5$ Pa s. The continuous (blue) line shows the time estimated with the Richardson and Zaki (1954) hindered settling model, the line with the circle symbols (red)

shows the equivalent but for the different hindered velocity used here (Eq. 20a), the line with cross symbols (yellow) shows results from a numerical simulation (outputs from Figure 7c) with our compaction correction to hindered settling and a maximum packing $X_m$ =0.63 and the purple line shows the same for the maximum close packing of spheres ($X_m$=0.74)..

## Conclusions

Particle settling is central to many fundamental processes in Earth and Planetary sciences. While the collective effect of particles on each other is known to affect the settling rate and has been parameterized as a hindrance function for many decades, we argue that the assumption that the settling rate is only function of the relative proportion of solids and fluid may fail to capture important dynamical behavior, particularly at high solid fractions. More specifically the existence and the growth of heterogeneities in particles spatial distribution (solid fraction) introduce an additional and traditionally overlooked contribution to energy dissipation through a stress term that introduces a consolidation or compaction viscosity.

This new consolidation or compaction term in the force balance causes remarkable dynamical features not seen with traditional hindered settling models. These features include the development of solid fraction waves at sharp fronts, with a structure that is controlled by a local balance between drag and compaction terms, in contrast with generic particle settling models where the force balance is restricted to drag and buoyancy. The balance between drag and compaction stresses introduces a characteristic length scale, the compaction length, into particle settling problems which affects the wavelength of the instability as well as the decay rate of the trailing waves behind the front.

We find that the resistance to compaction during particle settling (compaction viscosity) decreases significantly with decreasing solid fraction away from the maximum packing of particles, and that the strong dependence of the compaction viscosity on solid fraction allows generated waves to develop particle-depleted layers that grow over time. Thus, we expect that the compaction term introduced in particle settling not only generate dynamical waves at sharp fronts, but that these waves can cause bulk buoyancy and viscosity stratifications that may potentially initiate density overturns (Rayleigh-Taylor instability) if the growth rate of the latter exceeds the growth rate of the particle-depleted layer. This could affect convective heat and chemical transport at the top of magma bodies, where much of the heat driving crystallization occurs.

Another important feature associated with compaction term in the force balance relates to the growth and structure of particle cumulate layers at the base of closed systems, for example at the bottom of crystallizing magma bodies. The divergence of the compaction viscosity for settling at the maximum packing of the suspension caps the solid fraction at the maximum packing in the cumulate layer and slows the rate of settling (growth rate) of the cumulate layer compared to generic settling models.  This behavior seem supported by geochemical and

textural analyses of cumulate layers feeding high silica granites, where the minimum trapped melt has been shown to coincide with the maximum packing of cumulate crystal phases.

**References**


Bachmann, O., and Bergantz, G.W. (2004), On the origin of crystal-poor rhyolites: extracted from batholithic crystal mushes, Journal of Petrology, vol. 45, p. 1565-1582.

Bachmann, O., and Huber, C., (2016), Silicic magma reservoirs in the Earth's crust, American Mineralogist, vol. 101, p. 2377-2404.

Batchelor, G.K., An introduction to Fluid Dynamics, Cambridge University Press, 1970.

Bergantz, G.W., and Ni, J., (1999) A numerical study of sedimentation by dripping instabilities in viscous fluids, International Journal of Multiphase Flow, Vol. 25, p. 307-320.

Boukaré, C.-E., E.M. Parmentier, and S.W. Parman (2018) Timing of mantle overturn during magma ocean solidification, Earth Planet Sci Lett 491, 216-225 https://doi.org/10.1016/j.epsl.2018.03.037.

Bercovici, D., Y. Ricard, and G. Schubert (2001) A two phase model for damage and compaction, J. Geophys. Res. 106, 8887-8906.

Costa, A., L. Caricchi, and N. Bagdassarov (2009) A model for the rheology of particle-bearing suspensions and partially molten rocks, Geochem. Geophys. Geosys. 10 doi:10.1029/2008GC002138.

Culha C, Suckale, J., Keller, T., and Qin, Z., (2020) Crystal fractionation by crystal-driven convection, Geophysical Research Letters, vol. 47, e2019GLO86784.

Dasgupta, T., Mukherjee, S., (2020) Porosity in Carbonates. In: Sediment Compaction and Applications in Petroleum Geoscience. Advances in Oil and Gas Exploration & Production. Springer.

Davis, R.H., and Acrivos, A. , (1985), Sedimentation of noncolloidal particles at low Reynolds numbers, Ann. Rev. Fluid. Mech., vol. 17, p. 91-118.

Drew, D.A. (1983) Mathematical Modelling of Two Phase Flow, Ann. Rev. Fluid Mech. 15, 261-291.

Elkins-Tanton, L. T. (2012) Magma Oceans in the Inner Solar System, Ann. Rev Earth and Planet. Sci. 40:113-139, https://doi.org/10.1146/annurev-earth-042711-105503.

Fitch, B. (1983) Kynch theory and compression zones, AIChE J. 29, 940.

706 Faroughi, S.A., and Huber, C., Unifying the relative hindered velocity in suspensions and
707 emulsions of non-deformable particles, Geophysical Research Letters, vol. 42, 2015, p. 53-59.

708 Faroughi, S.A., and Huber, C., Rheological state variables: a framework for viscosity
709 parameterization in crystal-rich magmas, Journal of Volcanology and Geothermal Research, vol.
710 440, 2023, p. 107856.

711 Guazzelli, E., and Morris, J.F., A Physical Introduction to Suspension Dynamics, Cambridge
712 University Press, 2012.

713 Hess P.C. and E.M. Parmentier (1995) A model for the thermal and chemical evolution of the
714 Moon's interior: Implications for the onset of mare volcanism, Earth Planet Sci Lett 134, 501-
715 514. https://doi.org/10.1016/0012-821X(95)00138-3

716 Lee and Morton

717 Hildreth, W., and Wilson, C.J.N. (2007), Compositional zoning of the Bishop Tuff, Journal of
718 Petrology, vol. 48, p. 951-999.

719 Huguet, L., M. Le Bars, R. Deguen (2023) A laboratory model for iron snow in planetary cores,
720 Geophys. Res. Lett. 50, doi.org/10.1029/2023GL105697.

721 Kynch, G. J. (1952) ''A theory of sedimentation,'' Trans. Faraday Soc. 48, 166.

722 Lee, C.T.A. and D.M. Morton (2015) High silica granites: Terminal porosity and crystal settling in
723 shallow magma chambers, Earth Planet. Sci. Lett. 409, 23-31,
724 https://doi.org/10.1016/j.epsl.2014.10.040

725 Lister, J.R. and R.C. Kerr (1989) The effect of geometry on the gravitational instability of a
726 buoyant region of viscous fluid, J. Fluid Mech. 202, 577-594.

727 Lowman, N.K., and M.A. Hoeffer (2013) Dispersive shockwaves in a viscously deforming media,
728 J. Fluid Mech. 718, 524-557.

729 Marsh, B. and M. Maxey, On the distribution and separation of crystals in convecting magma,
730 Journal of Volcanology and Geothermal Research, 1985, V. 24, p. 95-150.

731 Martin, D., and Nokes, R., (1989) A fluid-dynamical study of crystal settling in convecting
732 magmas, Journal of Petrology, Vol. 30, p. 1471-1500.

733 McKenzie, D. (1984) The generation and compaction of partially molten rock, J. Petrology 25,
734 713-765.

735 Moore, C.H., (1989) Carbonate diagenesis and porosity. In: Developments in Sedimentology 46,
736 Elsevier.

737 Richardson J.F. and W.N. Zaki (1954) The sedimentation of a suspension of uniform spheres
738 under conditions of viscous flow, Chemical Engineering Science, Vol. 3, p. 65-73.

Rubie, D. C., H. J. Melosh, J. E. Reid, C. Liebske, and K. Righter (2003), Mechanisms of metal-silicate equilibration in the terrestrial magma ocean, *Earth Planet. Sci. Lett.*, 205, 239–255.

Shearer, C.K., et al., (2006) Thermal and magmatic evolution of the Moon, Reviews in Mineralogy and Geochemistry, 365-518.

Stevenson, D.J. (1990) Fluid dynamics of core formation, in: H. Newsom, J.H. Jones (Eds.), The Origin of the Earth, Oxford Press, London, pp. 231–249.

Solomatov, V.S. (2000) Fluid dynamics of magma oceans, Origin of the Earth and Moon (R. Canup, K. Righter, eds) Univ. of Arizona Press, Tucson 323-338.

Spiegelman, M., (1993) Flow in deformable porous media. J. Fluid Mech. 247, 39-63.

Stokes, G.G., On the effect of the internal friction of fluids on the motion of pendulums, Transactions of the Cambridge Philosophical Society, vol. IX, 1851, p[8]

Wallis, G.B., Two-phase flow, Dover Publications, 2020.

Whitehead, J.A. (1988) Fluid Models of Geological Hotspots, Ann. Rev. Fluid Mech. 20:61-87.

Wilcox and Whitehead (1991) Rayleigh-Taylor instability of an embedded low viscosity fluid layer, J. Geophys. Res. 96, 12193.

Zick, A.A., and Homsy, G.M., Stokes flow through a periodic array of spheres, Journal of Fluid Mechanics, vol. 115, 1982, p 13-26.

**Appendix 1:** Numerical methods

The mass and momentum conservation equations in one spatial dimension, (12) and (13), are solved using a finite standard volume formulation. Centered differences and linear interpolations are employed as required. Conservation of solid volume fraction (12) is solved using forward differences in time and conserving upwind approximations for advection. Numerical diffusion introduced by upwind approximations is minimized by using finely spaced grids in the simple one-dimensional problem. Most examples presented above were computed with 4096 grid points. Refinement to 8192 grid points showed at most a fraction of 1% change in computed values. An advantage of the upwind approximation is its simplicity and the stability of forward time stepping. The time step used was significantly less that the CFL time step to suppress numerical instability arising from time variable coefficients in the momentum equation.

**Appendix 2:** Nondimensionalization

773 The equations solved were expressed in nondimensional form based on an appropriate length
774 scale $L$ and single particle settling velocity $V_{stokes}$. Time in the solid phase conservation
775 equation is accordingly nondimensionalized $L/V_{stokes}$. The hindered settling velocity $V_H(X) =$
776 $V_{stokes}H(X)$ is derived from the hindrance function $H(X)$ and $V_{stokes}$ which is proportional to
777 the square of the particle size and inversely with the fluid viscosity $\mu_f$. For spherical particles is

778 $$V_{stokes} = \frac{2}{9}\frac{\Delta\varrho g a^2}{\mu_f}$$

779 The nondimensional momentum equation becomes

780 $$\frac{X}{(1-X)\,H(X)}V_s + X - \frac{V_{stokes}\mu_f}{\Delta\varrho g L^2}\frac{\partial}{\partial z}\left[X\frac{\zeta}{\mu_f}\frac{\partial V_s}{\partial z}\right] = 0$$

781 where $L$ may be an appropriate geometric length.

782 In the absence of such a length we choose

783 $$L \equiv \delta_{ref} = \sqrt{\frac{V_{stokes}\mu_f}{\Delta\varrho g}} = \frac{\sqrt{2}}{9}a$$

784 where $\delta_{ref}$ is a reference value of the compaction length removes all explicit nondimensional
785 parameters from both the momentum and solid fraction conservation equations.

786